

Article

# Squared Focal Intensity Distributions for Applications in Laser Material Processing

Henrike Schlutow<sup>1</sup>, Ulrike Fuchs<sup>1</sup> , Frank A. Müller<sup>2</sup> and Stephan Gräf<sup>2,\*</sup> 

<sup>1</sup> Asphericon GmbH, Stockholmer Str. 9, 07747 Jena, Germany; h.wilms@asphericon.com (H.S.); u.fuchs@asphericon.com (U.F.)

<sup>2</sup> Otto Schott Institute of Materials Research (OSIM), Friedrich Schiller University, Löbdergraben 32, 07743 Jena, Germany; frank.mueller@uni-jena.de

\* Correspondence: stephan.graef@uni-jena.de; Tel.: +49-3641-947754

**Abstract:** Tailored intensity profiles within the focal spot of the laser beam offer great potential for a well-defined control of the interaction process between laser radiation and material, and thus for improving the processing results. The present paper discusses a novel refractive beam-shaping element that provides different squared intensity distributions converted from the Gaussian output beam of the utilized femtosecond (fs) laser. Using the examples of surface structuring of stainless-steel on the micro- and nano-scale, the suitability of the beam-shaping element for fs-laser material processing with a conventional f-Theta lens is demonstrated. In this context, it was shown that the experimental structuring results are in good agreement with beam profile measurements and numerical simulations of the beam-shaping unit. In addition, the experimental results reveal the improvement of laser processing in terms of a significantly reduced processing time during surface nano-structuring and the possibility to control the ablation geometry during the fabrication of micro-channels.



**Citation:** Schlutow, H.; Fuchs, U.; Müller, F.A.; Gräf, S. Squared Focal Intensity Distributions for Applications in Laser Material Processing. *Materials* **2021**, *14*, 4981. <https://doi.org/10.3390/ma14174981>

Academic Editors: Jörg Krüger and Jörn Bonse

Received: 14 July 2021

Accepted: 27 August 2021

Published: 31 August 2021

**Publisher's Note:** MDPI stays neutral with regard to jurisdictional claims in published maps and institutional affiliations.



**Copyright:** © 2021 by the authors. Licensee MDPI, Basel, Switzerland. This article is an open access article distributed under the terms and conditions of the Creative Commons Attribution (CC BY) license (<https://creativecommons.org/licenses/by/4.0/>).

**Keywords:** beam shaping; squared top-hat; fs-laser; laser surface structuring; laser-induced periodic surface structures; micro-channels

## 1. Introduction

In modern laser material processing, beam shaping is receiving growing attention, as it allows the focal intensity distribution to be adjusted to the interaction process between the laser radiation and the material [1–3]. This makes laser processing even more flexible, precise and effective. Moreover, the range of achievable types of structures is extended [4–6] and surface properties can be adjusted in a targeted manner [7–9]. Top-hat profiles are characterized by a uniform intensity distribution over the beam cross-section in a specific working plane. They can be generated by a large variety of available beam-shaping techniques, including apertures [10], refractive [11–13] and diffractive optical elements [10,14], as well as beam integrators or homogenizers [10,15]. Finally, a spatial light modulator provides a flexible optical device that allows to create various intensity profiles based on the dynamical modification of the amplitude, phase and polarization of the incoming laser beam [16–18].

The advantage of refractive beam shapers is provided by their simple structure and a very high conversion efficiency. They are less sensitive to wavelength changes, easier to manufacture and can withstand higher laser powers when compared to diffractive elements. Therefore, the present work aims at the introduction of a highly flexible and compact refractive, freeform beam-shaping element that is suitable for laser material processing applications.

Large-area structuring of surfaces on the micro- and nano-meter scale usually requires scanning of the focused laser beam across the material surface. In the case of the commonly used Gaussian intensity distribution, a certain inhomogeneity of the deposited energy

occurs, which in turn has an influence on the processing result. A first improvement was demonstrated in this context by using a beam shaper that allows to generate a rotationally symmetric top-hat profile [19]. However, due to the rectangular symmetry of the (unidirectional) scan procedure with a specific overlap of the adjacent scan lines, the use of a squared top-hat seems to be even more advantageous with respect to homogeneous energy coupling. This squared top-hat is derived from the collimated Gaussian intensity profile of the input beam by combining the investigated refractive beam shaper with a focusing optics. The latter can be a simple focusing lens as well as a complex f-Theta objective, as is very often used for laser-based surface structuring. Therefore, a main objective of this study was to evaluate whether the x-y-symmetry of the focal distribution can further improve material processing when working with a scanner and an f-Theta lens. This aspect plays an essential role with regard to modern laser systems and their high repetition rates, whose maximum utilization ensures high processing efficiency. For this purpose, the beam-shaping element was practically tested in different applications on stainless-steel as a substrate material. This includes surface nano-structuring in the form of laser-induced periodic surface structures (LIPSS), which allow to engineer surfaces with versatile functional properties [7,20]. Furthermore, the ablation-based micro-structuring of the sample surface using femtosecond lasers (fs-lasers) was demonstrated as a conventional processing technique [21].

## 2. Materials and Methods

### 2.1. Focal Beam-Shaping and Characterization

The most common approach for shaping focal intensity distributions is based on Fourier optics, where the focusing optics transforms the incoming beam profile into the desired shape. This is well-explained for rotational symmetry in [19,22]. However, for non-rotationally symmetric focal intensity distributions, the symmetry of the beam-shaping element needs to be broken, while the focusing optics remains the same. Therefore, the beam-shaping element becomes a freeform surface. As a phase plate, it imprints a phase modulation on the incoming plan wave of the collimated beam, which stays collimated as this modulation is in the order of  $\lambda$  (PV) and thus very small. The focusing optics performs the Fourier transformation of this modified wave front and therefore determines the width of the generated profiles inverse proportional to the numerical aperture (NA). Consequently, this approach is modular with regards to the focusing optics. The phase plate (a |SqAiryShape) itself is a freeform distribution based on a super Gaussian profile:

$$z(h) = H e^{-2\left(\frac{4h^2}{D^2}\right)^{\frac{M}{2}}} \quad (1)$$

of order  $M = 8$ , diameter  $D$  and plateau height  $H$  in x-y-symmetry. The element is made of fused silica via CNC-based grinding and polishing. It can therefore withstand high-power laser intensities as well as ultrashort laser pulses, as employed in the experimental studies of the present work.

As a measure of how much the beam shaping will be affected by diffraction effects, the  $\beta$ -factor:

$$\beta = \frac{2\pi R D}{f_L \lambda} \quad (2)$$

can be used [23], with  $R$  being the half diameter of the entrance beam,  $D$  being the half diameter of the focal distribution,  $f_L$  being the focal length and  $\lambda$  being the wavelength. Using the specific parameters of the present study ( $R = 10$  mm,  $D = 25$   $\mu$ m,  $f_L = 100$  mm and  $\lambda = 1030$  nm) leads to  $\beta = 15.25$ . Having such a large value ensures stable beam-shaping profiles, which are essential for well-controlled material processing.

The squared focal intensity distribution was characterized in order to compare the experimental results with simulations. For this purpose, a supercontinuum laser (SC-400-4, Fianium, Southampton, UK) was used as a light source, from which  $\lambda = 1064$  nm was

selected via a spectrometer (LLTF Contrast, Fianium, Southampton, UK), coupled to a fiber, collimated (ACM25-20-L-C-1064, asphericon, Jena, Germany) and expanded (BAM25-175-D-C-1064, asphericon, Jena, Germany) to a collimated beam with 10 mm diameter. This beam fulfilled the input conditions for the freeform beam-shaping element. All following optical components used for characterization of the beam shaping are depicted in Figure 1. The beam-shaping element (a|SqAiryShape) was placed in the collimated beam, which was subsequently focused by a plano-convex lens with 300 mm focal length (#38-631, Edmund Optics, Mainz, Germany). The focal region was then imaged onto a camera (SP928, Ophir, Germany) by using a microscope objective (Aspheric Lens Kit 5720-B, Newport, Irvine, CA, USA). The setup was calibrated to obtain the real physical size of the focal distribution.

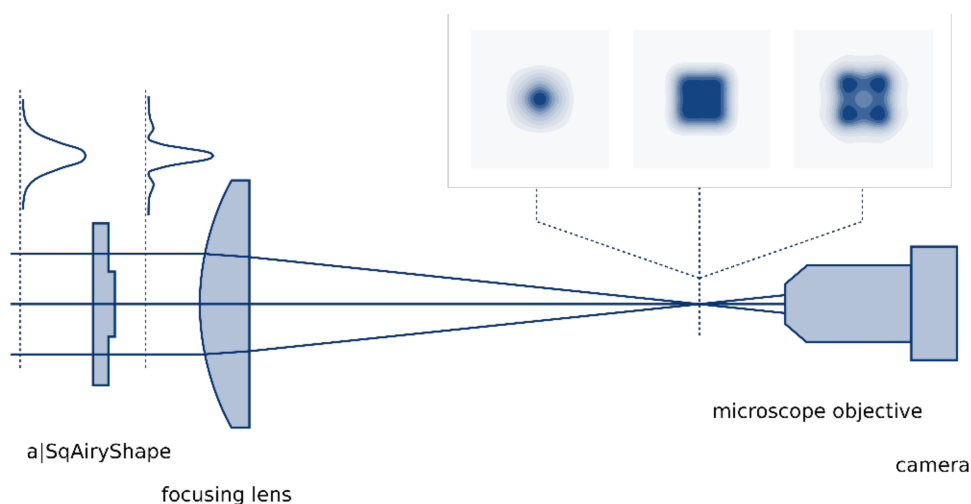


**Figure 1.** Experimental setup for characterization of the freeform beam-shaping element.

In the simulation, only the freeform beam-shaping element and the plano-convex focusing lens were considered. The focal intensity distribution was calculated via the point spread function with CodeV (Synopsis). This calculation is based on the squared Fourier transform of the pupil function [24]. The latter includes all aberrations and thus the phase manipulation introduced by the beam-shaping element.

Close to the focal point, various intensity distributions, such as a squared top-hat or squared donut, emerge. The following laser processing experiments were carried out with the squared top-hat, which occurs closest to the focal point. This is the top-hat shown in Figure 2. Comparison with the simulation, especially through the cross-sections in the bottom of Figure 2, reveals close agreement between measurement and simulation in terms of shape and size of the focus spot.

A sequence of those cross-sections taken along the optical axis is plotted in Figure 3. The upper panel (Figure 3a) shows the beam waist of the Gaussian input beam without the freeform beam-shaping element. With the beam-shaping element (panel b), the Gaussian distribution is notably flattened to a top-hat. Note that the beam shaping only occurs close to the focal point ( $z = 0$  mm), whereas the profile remains almost Gaussian for larger distances. The blue-shaded distribution corresponds to the one shown in Figure 2.

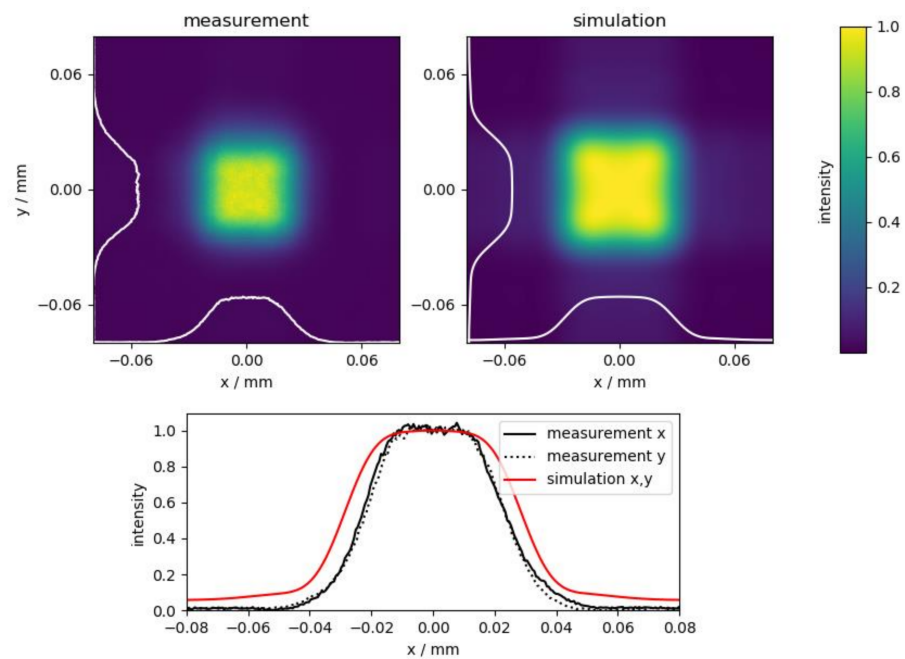


**Figure 2.** Color maps and cross-sections of the squared focal intensity distribution of the top-hat closest to the focal plane ( $\lambda = 1064$  nm,  $f = 300$  mm) normalized to the maximum intensity for comparison between measurement and simulation.

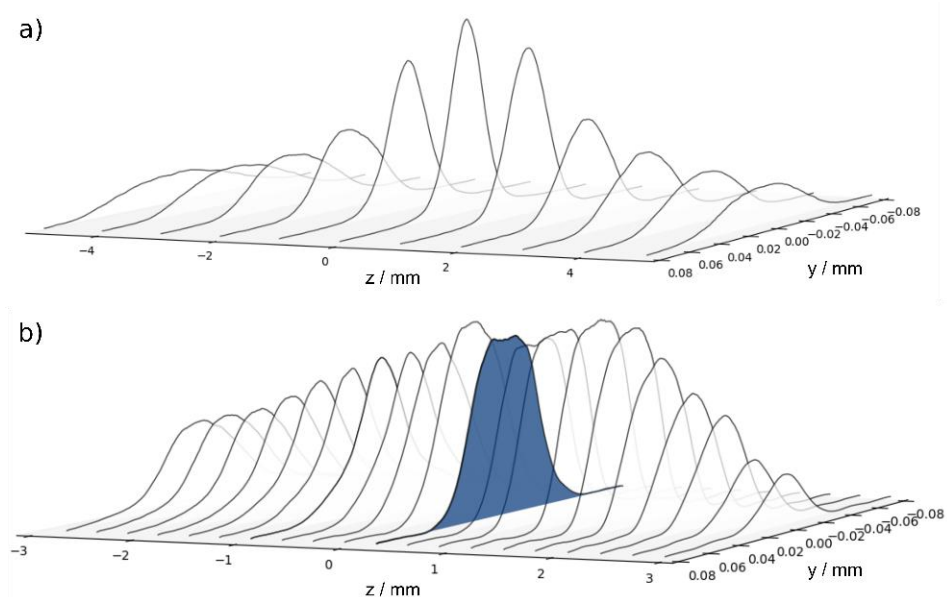


**Figure 3.** Profile cross-sections measured along the optical axis ( $z$ ) in the focal region (a) without and (b) with freeform beam-shaping element.

## 2.2. Material Processing Setup and Sample Preparation

The operation of the beam-shaping element was investigated by means of surface structuring experiments using the experimental setup illustrated in Figure 4. The linearly polarized Gaussian output beam ( $M^2 \sim 1.08$ ) of the diode-pumped Yb:KYW thin-disc fs-laser system (JenLas D2.fs, Jenoptik, Germany) with a central wavelength  $\lambda = 1025$  nm is characterized by a pulse duration  $\tau = 300$  fs (FWHM) and pulse energies  $E_{\text{imp}} \leq 40$   $\mu\text{J}$  at a repetition frequency  $f_{\text{rep}} = 100$  kHz. Before passing the beam shaper, the output beam was widened by a beam expander ( $5\times$ ). The shaped beam was then focused onto the

sample surface by a galvanometer scanner (IntelliScan14, Scanlab, Puchheim, Germany). The focal length of the associated f-Theta objective (JENar, Jenoptik, Jena, Germany) was  $f_L = 100$  mm.

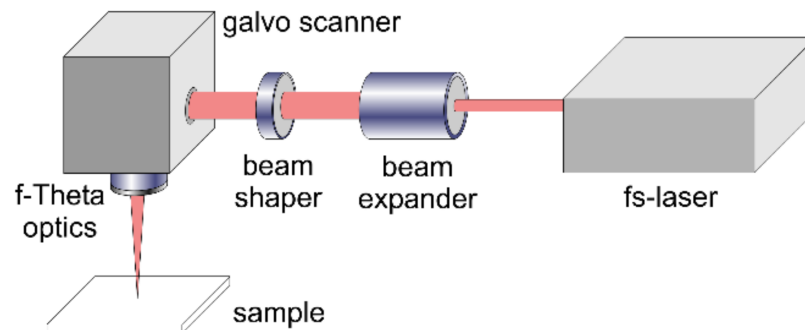


**Figure 4.** Experimental setup used for surface structuring experiments.

The structuring experiments were carried out on commercially available austenitic stainless-steel (X2CrNiMo17-12-2, Outokumpu, Krefeld, Germany) at normal incidence and under air atmosphere. Prior to laser irradiation, the sample surface was manually grounded and polished to a mirror finish, with an average surface roughness  $R_a \sim 4$  nm. This procedure involves the use of SiC abrasive paper of 800, 1200 and 2400 grit and 6, 3 and 1  $\mu\text{m}$  polycrystalline diamond suspension, respectively. Besides, the sample surfaces were ultrasonically cleaned in acetone and isopropanol both before and after laser structuring. The morphology of the samples was characterized by scanning electron microscopy (SEM) (SigmaVP, Carl Zeiss, Oberkochen, Germany) at an accelerating voltage of 5 kV using a secondary electron detector. The spatial periods and the orientation of the LIPSS were quantified by 2D-Fourier transform analysis (2D-FT) of the SEM micrographs. White light interference microscopy (WLIM) (CCI HD, Taylor Hobson, Weiterstadt, Germany) was utilized to evaluate the surface topography. The microscope was equipped with a  $50\times$  objective.

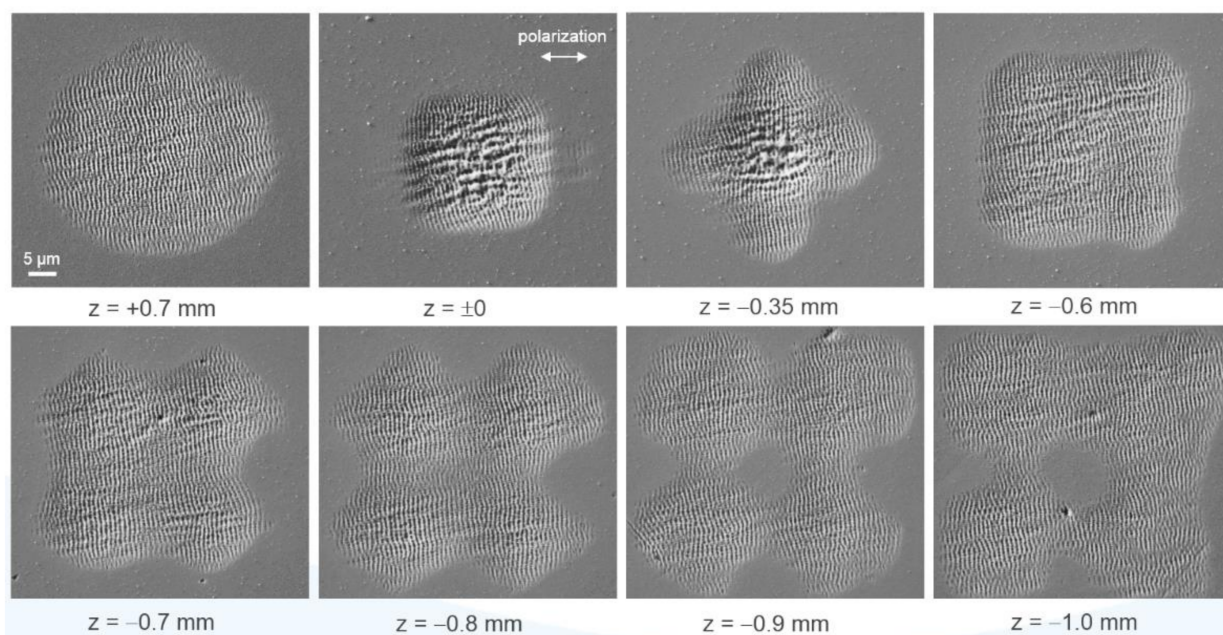
### 3. Results and Discussion

#### 3.1. Single-Spot Experiments

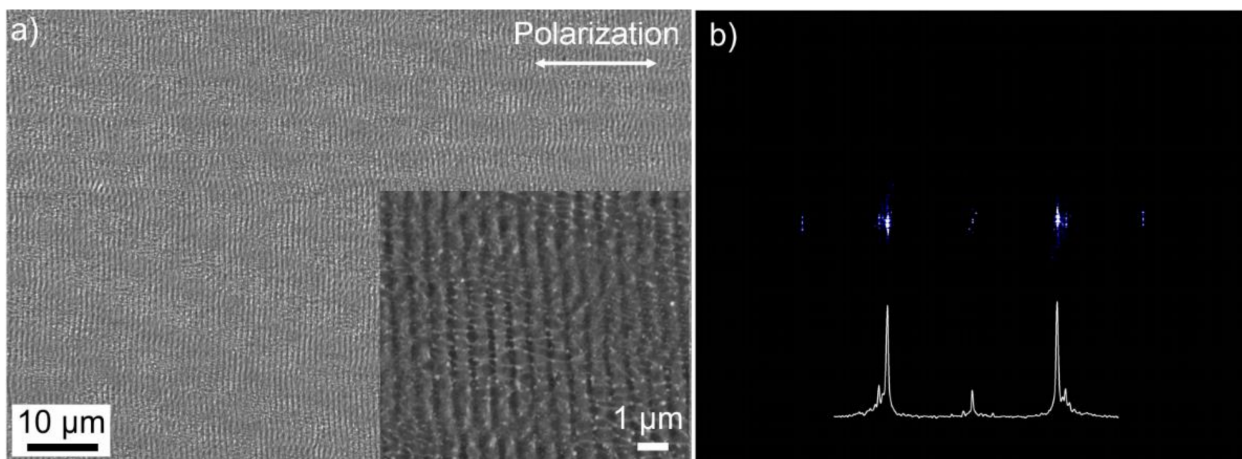
The first part of the experiments was to investigate whether the theoretical calculations for the focal intensity distribution correlate with the geometry of the ablated region within the focal spot on the material surface. For this purpose, the surface was irradiated with 10 single fs-laser pulses with a temporal pulse spacing of 10  $\mu\text{s}$  ( $f_{\text{rep}} = 100$  kHz) and a single-pulse energy of  $E_{\text{imp}} = 6.5$   $\mu\text{J}$ . Without the beam-shaping element in the beam path, the utilized f-Theta objective results in a focal spot diameter of  $2w_f = (24 \pm 0.5)$   $\mu\text{m}$ , determined using the method of Liu [25]. This corresponds to a fs-laser peak fluence of  $F = 2E_{\text{imp}}/(\pi w_f^2) = 2.9$   $\text{J}/\text{cm}^2$  at the pulse energy used.

Figure 5 shows SEM micrographs of the ablation spots obtained at different distances (z-positions) of the stainless-steel surface from the focusing objective using the freeform beam-shaping element. At the reference position ( $z = 0$  mm) and at  $z = -0.6$  mm, squared top-hat intensity profiles are available that result in square material ablation of size  $(30 \times 30)$   $\mu\text{m}^2$  and  $(40 \times 40)$   $\mu\text{m}^2$ , respectively. As described later, these intensity profiles are predestined for numerous laser material processes that are based on scanning procedures with x-y-symmetry (Figure 6). Assuming a perfectly rectangular fluence distribution of both top-hat profiles, the larger focal dimensions together with the pulse energy  $E_{\text{imp}} = 6.5$   $\mu\text{J}$  result in a lower fs-laser peak fluence of  $F = 0.72$  and  $F = 0.41$   $\text{J}/\text{cm}^2$  respectively, when compared to the initial Gaussian focal spot. It should be noted that the peak fluence,  $F$ , is identical to the average fluence,  $F_{\text{av}}$ , of the fluence distribution. The

larger fluence at  $z = 0$  compared to  $z = -0.6$  mm is indicated by the stronger melt formation in the ablation spot fabricated with the smaller top-hat profile.



**Figure 5.** SEM micrographs of the stainless-steel surface after irradiation of 10 linearly polarized single fs-laser pulses at different  $z$ -positions of the sample surface within the focal intensity distribution. For comparability, the single-pulse energy was kept constant at  $E_{\text{imp}} = 6.5 \mu\text{J}$ .



**Figure 6.** LIPSS structuring of stainless-steel surfaces using the squared top-hat profile ( $z = 0$  mm) of the linearly polarized fs-laser beam ( $2w_f \sim 30 \mu\text{m}$ ,  $E_{\text{imp}} = 3.5 \mu\text{J}$ ,  $v = 1$  m/s,  $\Delta x = 10 \mu\text{m}$ ): (a) SEM micrograph and (b) 2D-FT spectrum and its corresponding cross-section calculated from the SEM micrograph quantifying the homogeneity and orientation of the LIPSS.

In addition to the top-hat profiles, the beam-shaping element provides other intermediate stages, which are characterized by more exotic intensity distributions. At  $z = -1.0$  mm, a donut-shaped focal intensity distribution with square beam cross-section can be observed, characterized by the zero-intensity center on the beam axis. In contrast, at  $z = -0.35$  mm, the intensity distribution is almost completely reversed, which is why a stronger intensity can be observed at the center. Both examples are intensity distributions suitable for the generation of novel surface structures (e.g., bio-inspired surfaces) [5].

The SEM micrographs of the single-spot experiments reveal a well-defined modulated surface topography within the ablation crater, whose periodicity is in the sub- $\mu\text{m}$  range and therefore much smaller when compared to the diffraction-limited focal spot diameter

of a few tens of  $\mu\text{m}$ . These periodic patterns are termed laser-induced periodic surface structures (LIPSS), which for metals are typically oriented perpendicular to the linear beam polarization [26]. The most widely accepted theory describes the formation of LIPSS as a result of interference of the incident laser radiation with surface electromagnetic waves generated by scattering at the nano-rough surface [27,28]. These scattering processes are possible despite the polished initial surface, since the LIPSS formation process is generally a multi-pulse process.

As Figure 5 shows, the exact morphology of the LIPSS pattern within the focal spot depends on the fluence distribution in the beam cross-section, i.e., on the intensity profile. A particular contribution is provided by melt formation in the intensive regions of the beam cross-section. However, it becomes evident that a particularly homogeneous LIPSS distribution can be realized by the appropriate choice of the z-position, which suggests here a constant fluence in the beam profile. This is a key aspect for homogeneous large-area structuring with LIPSS [29]. In addition, the possibility to control the LIPSS distribution within the focal spot by choosing a certain beam profile leads to an extension of the current state-of-the-art and, thus, to a higher flexibility of the direct-writing structuring method. The fluence values calculated above for the top-hat profile are comparable with the fluence required for ablation-based LIPSS formation on stainless-steel at comparable irradiation parameters [30,31].

### 3.2. Laser Surface Structuring on the Nanoscale

Based on the demonstrated LIPSS formation within the focal spot, the nanostructures can be scaled to large surface areas by a relative movement between the focused fs-laser beam and the sample surface. This is particularly achievable with metals due to the linear absorption of the fs-laser radiation. In this context, the specific optical properties make stainless-steel a well-suited candidate for the production of highly regular LIPSS [31]. This concerns in particular the exact alignment and a small dispersion of the spatial frequencies of the LIPSS, which are coherently linked to each other despite the unidirectional scanning procedure [30,31].

The SEM micrograph in Figure 6a shows the stainless-steel surface obtained from scanning the squared top-hat profile ( $z = 0$  mm) with a scan speed of  $v = 1$  m/s and a line spacing of  $\Delta x = 10$   $\mu\text{m}$  across the sample surface. The single-pulse energy was reduced to  $E_{\text{imp}} = 3.5$   $\mu\text{J}$ , i.e., to  $F = 0.39$   $\text{J}/\text{cm}^2$ , in order to avoid the extensive melt formation observed in Figure 5. The calculated 2D-FT spectrum (Figure 6b) confirms the high regularity of the LIPSS aligned perpendicular to the linear beam polarization by the very narrow characteristic peaks. The spatial periods of the LIPSS were determined to be around  $(950 \pm 20)$  nm.

The obtained regularity is comparable with our previous work on rotationally symmetric beam shaping [19], although the following main differences should be discussed:

- (1) As already demonstrated in [30,31], highly regular LIPSS can also be generated with conventional Gaussian beam profiles. However, the radial intensity dependence and the circular spot area require a larger overlap of the laser pulses in both x- and y-directions to realize an almost homogeneous energy deposition. The optimal process parameters for Gaussian beam processing were derived in [19] to be  $v = 0.67$  m/s,  $\Delta x = 6$   $\mu\text{m}$ ,  $E_{\text{imp}} = 2.6$   $\mu\text{J}$ ,  $F = 1.15$   $\text{J}/\text{cm}^2$  at  $f_{\text{rep}} = 100$  kHz and  $2w_f = 24$   $\mu\text{m}$ . These values result in a processing rate of about  $32$   $\text{s}/\text{cm}^2$  and in a laser pulse number  $N_{\text{eff}_2\text{D}} = (\pi w_f^2 \cdot f_{\text{rep}}) / (v \cdot \Delta x) \sim 11.3$ , that effectively hit the focal spot area [28].
- (2) The main difference between the ideal squared top-hat and the Gaussian profile results from the relative movement during scanning. Figure 7a illustrates that for the Gaussian profile at a certain position  $y$  at the surface, every single pulse of the total required number ( $N_{\text{eff}_2\text{D}}$ ) contributes to structuring with different fluence values. Consequently, the specific fluence of some of the individual pulses can be significantly smaller than the ablation and LIPSS formation threshold of the material.

- (3) In the case of the top-hat profile ( $z = 0$ ) with its square shape, the slightly larger beam diameter (here given by the beam width in  $x$ - and  $y$ -directions) and steeper flanks, LIPSS structures with almost equal properties can be achieved. Nevertheless, the structuring can be performed with larger scanning speed ( $v = 1$  m/s) and line separation ( $\Delta x = 10$   $\mu\text{m}$ ). As described above, the pulse energy must be increased slightly for this to exceed the required LIPSS formation threshold. The optimum parameters, however, result in  $N_{\text{eff}_2\text{D}} = 9$  and a processing rate of about 14 s/cm<sup>2</sup>, which is more than a factor of 2 faster than structuring with the conventional Gaussian beam.
- (4) The accumulated fluence of the ideal top-hat profile with  $F_{\text{tot}} = N_{\text{eff}_2\text{D}} \cdot F = 3.51$  J/cm<sup>2</sup> is smaller than for the Gaussian intensity distribution ( $F_{\text{tot}} = 6.47$  J/cm<sup>2</sup>), since during structuring with the top-hat, each single pulse contributes equally to  $F_{\text{tot}}$  (Figure 7b).

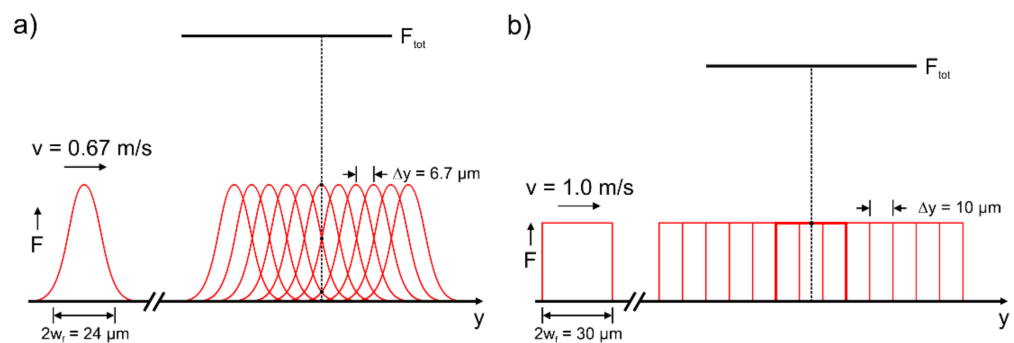


**Figure 7.** Overlap and contribution of individual pulses during scanning of a single line using (a) the Gaussian focal intensity distribution and (b) an ideal top-hat beam.

### 3.3. Surface Micro-Structuring

In order to investigate the influence of the intensity distribution on the micro-structuring of surfaces, channels were created using the top-hat profile ( $z = 0$  mm) and 10 over-scans with  $v = 0.1$  m/s. Earlier studies with rotationally symmetrical top-hat and donut-shaped beam profiles already showed that steeper channel walls and a better surface quality (especially at the bottom) can be achieved in comparison to the Gaussian profile [19].

These findings can also be observed in Figure 8, which shows 3D-WLIM micrographs of channels produced with the top-hat profile using different pulse energies,  $E_{\text{imp}}$ . It becomes evident for moderate pulse energies that the homogeneous fluence distribution across the beam profile leads to a very high quality of both the walls and the bottom of the channel (Figure 8a,b). The corresponding arithmetical roughness values of the channel surface were measured via WLIM to be  $S_a = 0.1072$   $\mu\text{m}$  for  $E_{\text{imp}} = 2.5$   $\mu\text{J}$  and  $S_a = 0.1844$   $\mu\text{m}$  for  $E_{\text{imp}} = 4.6$   $\mu\text{J}$ . As indicated by the cross-sections in Figure 8d, the corresponding depth of the channels increases with increasing pulse energy, from about 6.2  $\mu\text{m}$  at  $E_{\text{imp}} = 2.5$   $\mu\text{J}$  (Figure 8a) to about 12.5  $\mu\text{m}$  at  $E_{\text{imp}} = 7$   $\mu\text{J}$  (Figure 8c). In addition, a slight increase in the channel width can be observed. However, the WLIM micrographs indicate that at very high pulse energies and thus large laser peak fluences, an inhomogeneous and rough channel bottom results from extensive ablation and the melt formation already detected in the single-spot experiments. The irregularity is expressed in particular in hole-like depressions that are not adequately displayed by the perspective of the 3D micrograph in Figure 8c. However, a qualitative measure is given by the grey-shaded area in the cross-section of Figure 8d that illustrates the remarkably larger variation, especially at the channel bottom, when compared to smaller  $E_{\text{imp}}$ . This is also confirmed by the larger surface roughness that was measured to be  $S_a = 0.5174$   $\mu\text{m}$  for  $E_{\text{imp}} = 7$   $\mu\text{J}$ .

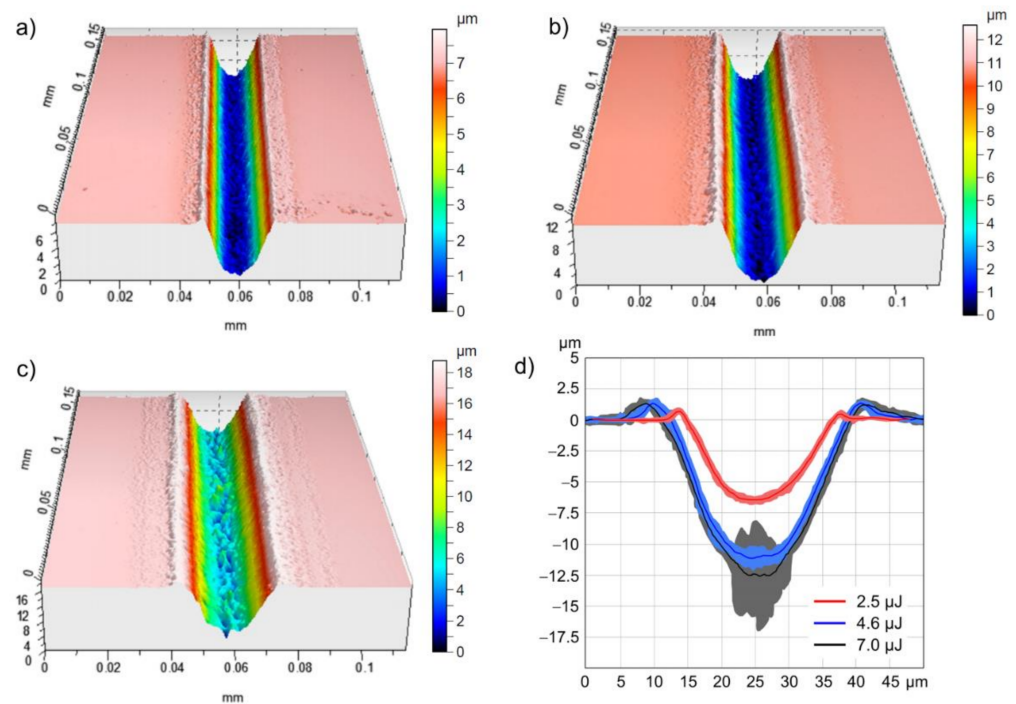


**Figure 8.** WLIM micrographs of the stainless-steel surface illustrating the 3D geometry of channel-like structures obtained from 10 over-scans with  $v = 0.1$  m/s using the squared top-hat profile at  $z = 0$  mm and different single-pulse energies: (a)  $E_{\text{imp}} = 2.5$   $\mu\text{J}$ , (b)  $E_{\text{imp}} = 4.6$   $\mu\text{J}$  and (c)  $E_{\text{imp}} = 7$   $\mu\text{J}$ . A comparison between the cross-sections of the channels is illustrated in (d). Here, the solid line corresponds to the mean profile and the shadow illustrates the variation of the profile series measured along the channel.

Structuring with the donut-shaped intensity profile at  $z = -0.9$  mm allows to create channels with steep walls and a w-shaped cross-sectional geometry that is determined by the specific intensity distribution (see Figure 5). According to the cross-sectional height profile of the channel (Figure 9c), 10 over-scans with  $v = 0.1$  m/s and  $E_{\text{imp}} = 4.6$   $\mu\text{J}$  result in a width of about 40  $\mu\text{m}$  and a maximum ablation depth of about 10  $\mu\text{m}$ . The channel walls are characterized by their very homogeneous and regular surfaces in the form of superimposed nanoscale LIPSS (Figure 9a). The high quality is confirmed by the fact that the modulation depth of LIPSS is typically in the order of 200 nm [30]. Contrary to a rotationally symmetrical donut, the used squared intensity profile provides the zero-intensity center and two axes in  $x$ - and  $y$ -directions with almost zero intensity. Consequently, the areas with lower (zero) intensity are not passed over by highly intensive beam parts during scanning in these directions, resulting in a channel with a less ablated central area (Figure 9b). This could be used, for example, to periodically propagate these w-shaped structures to large surface areas based on a suitable scan line distance. In dependence on the focal length of the focusing optics, this would result in a microscale periodic grating with periods in the range of 10–20  $\mu\text{m}$ . Similar surface structures with comparable structural sizes can be obtained, e.g., from Direct Interference Laser Patterning, which is used among others to generate surfaces with functional properties (optics, tribology, biology, wetting) [32].

Generally, the results show that the donut and top-hat profiles provided by the beam-shaping element are advantageous for realizing micro-channels with specific wall inclination angles as well as tailor-made cross-sectional geometry. This option is also available (in situ) during the structuring process, since the individual intensity profiles can be addressed in a relatively simple way by changing the  $z$ -position of the sample surface.

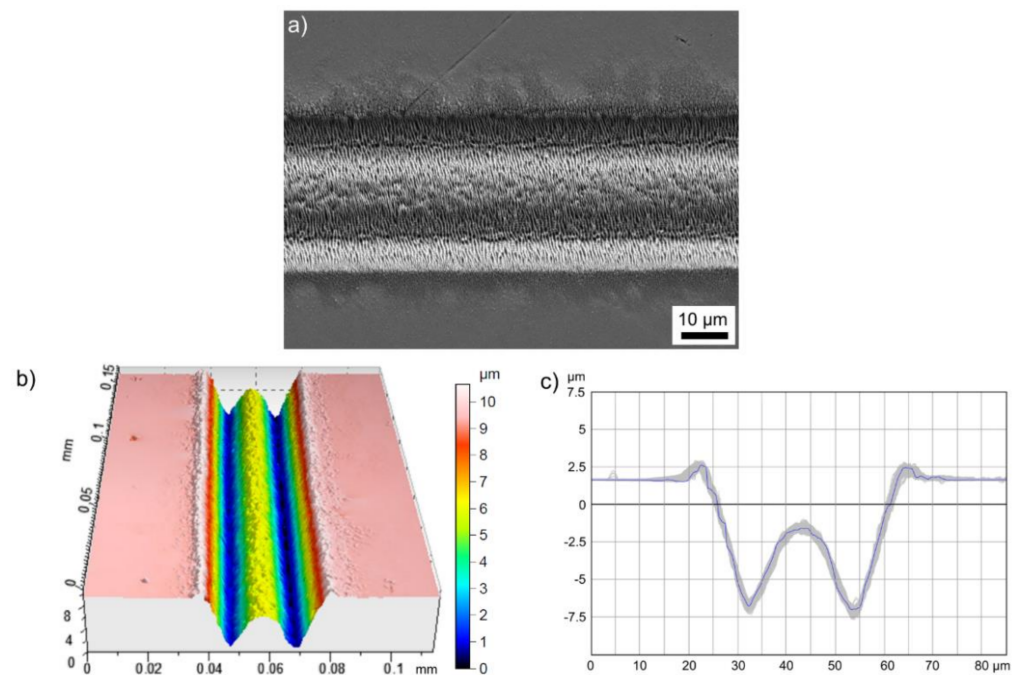


**Figure 9.** Micro-channel fabricated on stainless-steel using the squared donut-like intensity distribution at  $z = -0.9$  mm, 10 over-scans with  $v = 0.1$  m/s and a single-pulse energy of  $4.6 \mu\text{J}$ : (a) SEM micrograph, (b) WLIM micrograph and (c) cross-sectional height profile. The blue line in (c) corresponds to the mean profile and the grey shadow illustrates the profile series measured along the channel in (b).

#### 4. Conclusions

The present study deals with a versatile refractive beam shaper that allows to convert the initial Gaussian intensity distribution of the fs-laser beam into different squared beam profiles at different  $z$ -positions. Numerical simulations for the beam-shaping unit were verified experimentally by spatial beam profile measurements and by surface structuring on the micro- and nano-scale. It was demonstrated that the squared top-hat profiles available in the focal region are advantageous to significantly reduce the processing time during large-area LIPSS structuring, while preserving their high regularity. Using the beam shaper for the generation of channel-like structures via multiple line scans, it was shown that the different focal intensity distributions resulted in precise channels with a controllable cross-sectional geometry.

**Author Contributions:** All authors contributed equally to conceptualization, methodology, validation, writing—original draft preparation, and visualization. All authors have read and agreed to the published version of the manuscript.

**Funding:** This research received no external funding.

**Institutional Review Board Statement:** Not applicable.

**Informed Consent Statement:** Not applicable.

**Data Availability Statement:** The data underlying this article will be shared on reasonable request from the corresponding author.

**Conflicts of Interest:** The authors declare no conflict of interest.

## References

1. Malinauskas, M.; Zukauskas, A.; Hasegawa, S.; Hayasaki, Y.; Mizeikis, V.; Buividas, R.; Juodkazis, S. Ultrafast laser processing of materials: From science to industry. *Light-Sci. Appl.* **2016**, *5*, e16133. [[CrossRef](#)]
2. Raciukaitis, G.; Stankevicius, E.; Gecys, P.; Gedvilas, M.; Bischoff, C.; Jager, E.; Umhofer, U.; Volklein, F. Laser processing by using diffractive optical laser beam shaping technique. *J. Laser Micro Nanoen.* **2011**, *6*, 37–43. [[CrossRef](#)]
3. Sugioka, K.; Cheng, Y. A tutorial on optics for ultrafast laser materials processing: Basic microprocessing system to beam shaping and advanced focusing methods. *Adv. Opt. Technol.* **2012**, *1*, 353. [[CrossRef](#)]
4. Allegre, O.J.; Jin, Y.; Perrie, W.; Ouyang, J.; Fearon, E.; Edwardson, S.P.; Dearden, G. Complete wavefront and polarization control for ultrashort-pulse laser microprocessing. *Opt. Express* **2013**, *21*, 21198–21207. [[CrossRef](#)]
5. Skoulas, E.; Manousaki, A.; Fotakis, C.; Stratakis, E. Biomimetic surface structuring using cylindrical vector femtosecond laser beams. *Sci. Rep.* **2017**, *7*, 45114. [[CrossRef](#)]
6. Ouyang, J.; Perrie, W.; Allegre, O.J.; Heil, T.; Jin, Y.; Fearon, E.; Eckford, D.; Edwardson, S.P.; Dearden, G. Tailored optical vector fields for ultrashort-pulse laser induced complex surface plasmon structuring. *Opt. Express* **2015**, *23*, 12562–12572. [[CrossRef](#)] [[PubMed](#)]
7. Müller, F.A.; Kunz, C.; Gräf, S. Bio-inspired functional surfaces based on laser-induced periodic surface structures. *Materials* **2016**, *9*, 476. [[CrossRef](#)]
8. Gräf, S. Formation of laser-induced periodic surface structures on different materials: Fundamentals, properties and applications. *Adv. Opt. Technol.* **2020**, *9*, 11–39. [[CrossRef](#)]
9. Stratakis, E.; Bonse, J.; Heitz, J.; Siegel, J.; Tsibidis, G.; Skoulas, E.; Papadopoulos, A.; Mimidis, A.; Joel, A.-C.; Comanns, P. Laser engineering of biomimetic surfaces. *Mater. Sci. Eng. R Rep.* **2020**, *141*, 100562. [[CrossRef](#)]
10. Dickey, F.M. Theory and techniques for laser beam shaping. *Int. Congr. Appl. Lasers Electro.-Opt.* **2001**, *2001*, 1393–1402.
11. Frieden, B.R. Lossless conversion of a plane laser wave to a plane wave of uniform irradiance. *Appl. Opt.* **1965**, *4*, 1400–1403. [[CrossRef](#)]
12. Rhodes, P.W.; Shealy, D.L. Refractive optical systems for irradiance redistribution of collimated radiation—Their design and analysis. *Appl. Opt.* **1980**, *19*, 3545–3553. [[CrossRef](#)] [[PubMed](#)]
13. Hoffnagle, J.A.; Jefferson, C.M. Design and performance of a refractive optical system that converts a gaussian to a flattop beam. *Appl. Opt.* **2000**, *39*, 5488–5499. [[CrossRef](#)] [[PubMed](#)]
14. Veldkamp, W.B.; Kastner, C.J. Beam profile shaping for laser radars that use detector arrays. *Appl. Opt.* **1982**, *21*, 345–356. [[CrossRef](#)]
15. Bollanti, S.; Di Lazzaro, P.; Murra, D. More about the light beam shaping by the integration method. *Eur. Phys. J.-Appl. Phys.* **2004**, *28*, 179–186. [[CrossRef](#)]
16. Häfner, T.; Strauss, J.; Roeder, C.; Heberle, J.; Schmidt, M. Tailored laser beam shaping for efficient and accurate microstructuring. *Appl. Phys. A Mater. Sci. Process.* **2018**, *124*, 111. [[CrossRef](#)]
17. Li, J.; Kuanga, Z.; Vilara, J.G.; Deardena, G.; Perrie, W.; Edwardson, S. Dynamic ultrafast laser beam shaping for material processing at the imaging plane using a spatial light modulator. In Proceedings of the 9th International Conference on Photonic Technologies LANE, Gurth, Germany, 19–22 September 2016.
18. Jin, Y.; Allegre, O.J.; Perrie, W.; Abrams, K.; Ouyang, J.; Fearon, E.; Edwardson, S.P.; Dearden, G. Dynamic modulation of spatially structured polarization fields for real-time control of ultrafast laser-material interactions. *Opt. Express* **2013**, *21*, 25333–25343. [[CrossRef](#)]
19. Möhl, A.; Kaldun, S.; Kunz, C.; Müller, F.A.; Fuchs, U.; Gräf, S. Tailored focal beam shaping and its application in laser material processing. *J. Laser Appl.* **2019**, *31*, 042019. [[CrossRef](#)]
20. Bonse, J.; Kirner, S.V.; Höhm, S.; Epperlein, N.; Spaltmann, D.; Rosenfeld, A.; Krüger, J. Applications of laser-induced periodic surface structures (lipss). *Proc. SPIE* **2017**, *10092*, 100920N.
21. Sugioka, K.; Meunier, M.; Piqué, A. *Laser Precision Microfabrication*; Springer: Berlin, Germany, 2010.
22. Cordingley, J.J. Method for Severing Integrated-Circuit Connection Paths by a Phase-Plate-Adjusted Laser Beam. U.S. Patent 5,300,756, 22 October 1991.
23. Dickey, F.M. *Laser Beam Shaping: Theory and Techniques*, 2nd ed.; CRC Press, Taylor & Francis Group: Boca Raton, FL, USA, 2014.
24. Hopkins, H.H.; Yzuel, M.J. The computation of diffraction patterns in the presence of aberrations. *Opt. Acta Int. J. Opt.* **1970**, *17*, 157–182. [[CrossRef](#)]
25. Liu, J.M. Simple technique for measurements of pulsed gaussian beam spot sizes. *Opt. Lett.* **1982**, *7*, 196–198. [[CrossRef](#)] [[PubMed](#)]
26. Bonse, J.; Krüger, J.; Höhm, S.; Rosenfeld, A. Femtosecond laser-induced periodic surface structures. *J. Laser Appl.* **2012**, *24*, 042006. [[CrossRef](#)]
27. Sipe, J.E.; Young, J.F.; Preston, J.S.; van Driel, H.M. Laser-induced periodic surface structure. I. Theory. *Phys. Rev. B* **1983**, *27*, 1141–1154. [[CrossRef](#)]
28. Bonse, J.; Gräf, S. Maxwell meets marangoni—a review of theories on laser-induced periodic surface structures. *Laser Photon. Rev.* **2020**, *14*, 2000215. [[CrossRef](#)]
29. Kunz, C.; Engel, S.; Müller, F.A.; Gräf, S. Large-area fabrication of laser-induced periodic surface structures on fused silica using thin gold layers. *Nanomaterials* **2020**, *10*, 1187. [[CrossRef](#)]

30. Gräf, S.; Kunz, C.; Undisz, A.; Wonneberger, R.; Rettenmayr, M.; Müller, F.A. Mechano-responsive colour change of laser-induced periodic surface structures. *Appl. Surf. Sci.* **2019**, *471*, 645–651. [[CrossRef](#)]
31. Gnilitzkyi, I.; Derrien, T.J.Y.; Levy, Y.; Bulgakova, N.M.; Mocek, T.; Orazi, L. High-speed manufacturing of highly regular femtosecond laser-induced periodic surface structures: Physical origin of regularity. *Sci. Rep.* **2017**, *7*, 8485. [[CrossRef](#)]
32. Müller, D.W.; Fox, T.; Grützmacher, P.G.; Suarez, S.; Mücklich, F. Applying ultrashort pulsed direct laser interference patterning for functional surfaces. *Sci. Rep.* **2020**, *10*, 3647. [[CrossRef](#)] [[PubMed](#)]